

# Detailed microscopic calculation of stellar electron and positron capture rates on $^{24}\text{Mg}$ for O+Ne+Mg core simulations

Jameel-Un Nabi

Faculty of Engineering Sciences, GIK Institute of Engineering Sciences and Technology, Topi 23640, NWFP, Pakistan

Current Address: ICTP, Strada Costiera 11, 34014, Trieste, Italy

E-mail: jnabi00@gmail.com

**Abstract.** Few white dwarfs, located in binary systems, may acquire sufficiently high mass accretion rates resulting in the burning of carbon and oxygen under nondegenerate conditions forming a O+Ne+Mg core. These O+Ne+Mg cores are gravitationally less bound than more massive progenitor stars and can release more energy due to the nuclear burning. They are also amongst the probable candidates for low entropy r-process sites. Recent observations of subluminous Type II-P supernovae (e.g., 2005cs, 2003gd, 1999br, 1997D) were able to rekindle the interest in 8 – 10  $M_{\odot}$  which develop O+Ne+Mg cores. Microscopic calculations of capture rates on  $^{24}\text{Mg}$ , which may contribute significantly to the collapse of O+Ne+Mg cores, using shell model and proton-neutron quasiparticle random phase approximation (pn-QRPA) theory, were performed earlier and comparisons made. Simulators, however, may require these capture rates on a fine scale. For the first time a detailed microscopic calculation of the electron and positron capture rates on  $^{24}\text{Mg}$  on an extensive temperature-density scale is presented here. This type of scale is more appropriate for interpolation purposes and of greater utility for simulation codes. The calculations are done using the pn-QRPA theory using a separable interaction. The deformation parameter, believed to be a key parameter in QRPA calculations, is adopted from experimental data to further increase the reliability of the QRPA results. The resulting calculated rates are up to a factor of 14 or more enhanced as compared to shell model rates and may lead to some interesting scenario for core collapse simulators.

PACS numbers: 26.50.+x, 23.40.Bw, 23.40.-s, 21.60Jz

## 1. Introduction

White dwarfs located in a binary system may end their lives in two possible ways. They may accrete from a companion and achieve the Chandrasekhar mass thereby triggering a thermonuclear runaway of the object and ultimately exploding as a Type Ia supernova. In this case no remnant is left behind. Alternatively these massive white dwarfs, for sufficiently high mass accretion rates, may allow the formation of O+Ne+Mg cores and due to the high prevailing central density (beyond  $10^{10}\text{gcm}^{-3}$ ) experience rapid electron capture that lead to the collapse of the core [1]. This is termed as accretion-induced collapse (AIC). The end product is a neutron star (in some double-degenerate scenario, two white dwarfs in a short-period binary system may eventually coalesce to form a massive white dwarf that exceeds the Chandrasekhar mass limit and in this case transition to a black hole is possible if the total proto-neutron star mass exceeds the general-relativistic limit for gravitational stability [2]). The ultimate fate of these white dwarfs are dependent on many factors, e.g. temperature of the environment, the mass accretion rate on the newly formed white dwarf, and the mass of each partner white dwarf [2]. The occurrence rate of the AIC of white dwarfs is not determined reliably, and are not expected to occur more than once per 20 – 50 standard Type Ia events (see for example [2]).

Supernova explosions from the collapse of O+Ne+Mg cores remain a potential research interest for astrophysical reasons. Its smaller core and smaller gravitational potential may allow the star to explode hydrodynamically. They are also proposed as a probable candidate for the site of r-process as compared to the "neutrino wind" mechanism based on the condition that they may explode by the prompt bounce-shock mechanism [2-5]. A detailed analysis of the core evolution of massive stars may be found in [1].

The evolution of the stars in the mass range  $8 - 10 M_{\odot}$  develops central cores which are composed of  $^{16}\text{O}$ ,  $^{20}\text{Ne}$  and  $^{24}\text{Mg}$ . Oda et al. [6] employed shell model wave functions of the *sd*-shell nuclei developed by Wildenthal [7] and calculated the capture rates which contribute to the collapse of the O+Ne+Mg core. Oda et al. [6] pointed out three different series of electron capture in the O+Ne+Mg core of the  $8 - 10 M_{\odot}$  stars and placed them in the order of low threshold energy as  $^{24}\text{Mg} \rightarrow ^{24}\text{Na} \rightarrow ^{24}\text{Ne}$ ,  $^{20}\text{Ne} \rightarrow ^{20}\text{F} \rightarrow ^{20}\text{O}$ , and  $^{16}\text{O} \rightarrow ^{16}\text{N} \rightarrow ^{16}\text{C}$ . They, however, renounced the last series in their calculations because of its high threshold energy which did not contribute significantly to the initiation of the collapse of the O+Ne+Mg core of the  $8 - 10 M_{\odot}$  stars.

A reasonably large number of recent observations and accumulation of data regarding Type II-P supernovae lead to a rejuvenation of debate on the fate of O+Ne+Mg cores. Earlier Gutiérrez et al. [8] argued that the abundance of  $^{24}\text{Mg}$  was considerably reduced in updated evolutionary calculations. However the procedure adopted by them was not fully consistent as they kept the ratio of oxygen to neon constant while parameterizing the abundance of  $^{24}\text{Mg}$ . Later Kitaura et al. [9] presented simulation result of these cores (keeping capture rates on  $^{24}\text{Mg}$  as a key ingredient)

using an improved neutrino transport treatment. Their outcome was not a prompt but a delayed explosion. Kitaura and collaborators [9] used the shell model capture rates of Takahara et al. [10] as a key nuclear input parameter in their simulation codes in the non-nuclear statistical equilibrium regime. One of the reasons for this spherical core collapse simulations not to explode was the reduced electron capture rates employed in their simulations. This reduced capture rate slowed the collapse process and resulted in a large shock radius.

Electron captures on proton and positron captures on neutron play a very crucial role in the supernovae dynamics. During the collapse and accretion phases, these processes exhaust electrons, thus decreasing the degenerate pressure of electrons in the stellar core. Meanwhile, they produce neutrinos which carry the binding energy away. Therefore, electron and positron captures play key role in the dynamics of the formation of bounce shock of supernova. The Type II supernovae take place in heavy stars. The positron captures are of great importance in high temperature and low density locations. In such conditions, a rather high concentration of positron can be reached from  $e^- + e^+ \leftrightarrow \gamma + \gamma$  equilibrium favoring the  $e^- e^+$  pairs. The electron captures on proton and positron captures on neutron are considered important ingredients in the modeling of Type II supernovae [11].

The key purpose of reporting this work is the presentation of the newly calculated microscopic calculation of the electron and positron capture rates using the pn-QRPA theory with separable interaction. Due to the extreme conditions prevailing in the cores of O+Ne+Mg stars, interpolation of calculated rates within large intervals of temperature-density points posed some uncertainty in the values of capture rates for collapse simulators. As such the calculation is done on a detailed temperature and density grid pertinent to presupernova and supernova environment and should prove more suitable for running on simulation codes.

The pn-QRPA theory is proven to be quite successful in the calculation of stellar weak rates. Earlier Nabi and Klapdor [12] used the pn-QRPA theory to calculate the weak interaction rates for 178 *sd*-shell nuclei [12] and 650 fp/fpg-shell [13] nuclide in stellar matter. The reliability of the pn-QRPA calculations was discussed in detail by Nabi and Klapdor [13]. There the authors compared the measured data (half lives and Gamow-Teller (GT) strength) of thousands of nuclide with the pn-QRPA calculations and got fairly good comparison. Later the decay and capture rates of nuclei of astrophysical importance were studied separately in detail and were compared with earlier calculations wherever possible both in *sd*-shell [14] and fp-shell (e.g. [15-17]) regions. Compared to shell model calculations, the pn-QRPA gives similar accuracy in reproducing beta-decay and capture rates in *sd*-shell nuclei [14]. The deformation parameter is as an important parameter for QRPA calculations as pairing [18]. For the case of even-even nuclei, experimental deformations are available [19] and were employed in this work.

In this paper a detailed calculation of electron and positron capture rates on  $^{24}\text{Mg}$  is being presented for the first time at temperature-density intervals suitable for simulation

purposes. The presence of  $^{24}\text{Mg}$  in the core is a result of the previous phase of carbon burning and its relevance is due to its lower electron capture threshold. Section 2 briefly discusses the formalism of the pn-QRPA calculations. Section 3 presents some of the calculated results. Comparison with earlier calculations is also included in this section. The conclusions are given in Section 4 and at the end Table 1 presents the detailed calculation of electron and positron capture rates on  $^{24}\text{Mg}$ .

## 2. Formalism

The Hamiltonian for the calculations was chosen to be of the form

$$H^{QRPA} = H^{sp} + V^{pair} + V_{GT}^{ph} + V_{GT}^{pp}, \quad (1)$$

where  $H^{sp}$  is the single-particle Hamiltonian,  $V^{pair}$  is the pairing force,  $V_{GT}^{ph}$  is the particle-hole (ph) Gamow-Teller force, and  $V_{GT}^{pp}$  is the particle-particle (pp) Gamow-Teller force. Single particle energies and wave functions were calculated in the Nilsson model, which takes into account nuclear deformations. Pairing was treated in the BCS approximation. The proton-neutron residual interactions occurred as particle-hole and particle-particle interaction. The interactions were given separable form and were characterized by two interaction constants  $\chi$  and  $\kappa$ , respectively. In this work, the values of  $\chi$  and  $\kappa$  was taken as 0.001 MeV and 0.05 MeV, respectively. Other parameters required for the calculation of weak rates are the Nilsson potential parameters, the deformation, the pairing gaps, and the Q-value of the reaction. Nilsson-potential parameters were taken from Ref. [20] and the Nilsson oscillator constant was chosen as  $\hbar\omega = 41A^{-1/3}(\text{MeV})$  (the same for protons and neutrons). The calculated half-lives depend only weakly on the values of the pairing gaps [21]. Thus, the traditional choice of  $\Delta_p = \Delta_n = 12/\sqrt{A}(\text{MeV})$  was applied in the present work. The deformation parameter is recently argued to be one of the most important parameters in QRPA calculations [18] and as such rather than using deformations from some theoretical mass models (as used in earlier calculations of pn-QRPA capture rates) the experimentally adopted value of the deformation parameters for  $^{24}\text{Mg}$ , extracted by relating the measured energy of the first  $2^+$  excited state with the quadrupole deformation, was taken from Raman et al. [19]. Q-values were taken from the recent mass compilation of Audi et al. [22].

The electron capture (ec) and positron capture (pc) rates of a transition from the  $i$ th state of the parent to the  $j$ th state of the daughter nucleus is given by

$$\lambda_{ij}^{ec(pc)} = \left[ \frac{\ln 2}{D} \right] [f_{ij}(T, \rho, E_f)] \left[ B(F)_{ij} + \left( \frac{g_A}{g_V} \right)^2 B(GT)_{ij} \right]. \quad (2)$$

The value of D was taken to be 6295s [23] and the ratio of the axial vector to the vector coupling constant as -1.254 [24].  $B'_{ij}$ s are the sum of reduced transition probabilities of the Fermi B(F) and GT transitions B(GT). The  $f'_{ij}$ s are the phase space integrals. Details of the calculations of phase space integrals, reduced transition probabilities and choice of Gamow-Teller strength parameters can be found in [12,13,25].

The total electron (positron) capture rate per unit time per nucleus was then calculated using

$$\lambda^{ec(pc)} = \sum_{ij} P_i \lambda_{ij}^{ec(pc)}. \quad (3)$$

The summation over all initial and final states was carried out until satisfactory convergence in the rate calculations was achieved. Here  $P_i$  is the probability of occupation of parent excited states and follows the normal Boltzmann distribution.

It is pertinent to mention that experimental data was incorporated in the calculations wherever possible to further increase the reliability of the calculated capture rates. In addition to the incorporation of the measured value of the deformation parameter, the calculated excitation energies (along with their  $\log ft$  values) were replaced with an experimental one when they were within 0.5 MeV of each other. Missing measured states were inserted and inverse and mirror transitions were also taken into account. No theoretical levels were replaced with the experimental ones beyond the excitation energy for which experimental compilations have no definite spin and/or parity. This means that no theoretical levels were replaced in the parent  $^{24}\text{Mg}$  beyond 9.3 MeV. For the daughter nuclei no replacement was done in  $^{24}\text{Na}$  beyond 1.3 MeV (for the electron capture direction) and in  $^{24}\text{Al}$  beyond 1.1 MeV (for the positron capture direction).

### 3. Results and Discussions

The Gamow-Teller strength distributions,  $B(\text{GT}\pm)$ , and the associated electron and positron capture rates on  $^{24}\text{Mg}$  were calculated using the pn-QRPA theory. Quenching of the GT strength was taken into account and a standard quenching factor of 0.77 was used [26]. The calculation was performed for a total of 132 excited states of  $^{24}\text{Mg}$  up to excitation energies in the vicinity of 40 MeV (corresponding to first 100 excited states) in the daughters  $^{24}\text{Na}$  and  $^{24}\text{Al}$ .

The summed  $B(\text{GT}+)$  strength is shown in Fig.1. It is to be noted that the experimentally extracted total  $B(\text{GT}+)$  strength for excitation energy region up to 7 MeV (where the density of states is still low enough to analyze single peaks) is 1.36 [27]. The corresponding calculated value reported in this work comes to be 2.53. The earlier reported pn-QRPA value was 2.65 [14]. The differences in the  $B(\text{GT}+)$  value and in the calculated capture rates compared to those of Ref. [14] are attributed primarily to the choice of deformation parameter and incorporation of all experimental levels (along with their  $\log ft$  values, if available) as stated in previous section. Whereas the authors in [14] incorporated a deformation parameter of 0.435 according to the mass formula of Möller and Nix [28], in this work the measured value of 0.606 [19] is taken to be the deformation parameter for  $^{24}\text{Mg}$ . Details on the sensitivity of  $B(\text{GT}+)$  strength as a function of deformation parameter can be found in [29]. Regarding the measured value of the GT strength, it is to be noted that Rakers and collaborators [27] employed a  $sd$ -model space and the universal  $sd$  residual interaction [30,31] to calculate

the wave functions. The authors in [27] argued that the full model space calculation was not possible and they had to truncate the model space which subsequently lead to uncertainties and the authors had some reservations in the interpretation of their data. The pn-QRPA value reported in this work is close to the reported shell model value of 2.1 of Brown and Wildenthal [30] and Wildenthal [31]. Takahara et al. [10] reported a value of 1.30. The total calculated GT strength in this work is 3.34 (quenched).

Fig.2 depicts the summed B(GT-) strength as a function of excitation energies in the daughter nucleus  $^{24}\text{Al}$ . The total strength comes to 3.34 (quenched) and the Ikeda sum rule is fulfilled in the calculations.

Moving on to the calculation of capture rates, Fig.3 shows four panels depicting the calculated electron capture rates at selected temperature and density domain. The upper left panel shows the electron capture rates in low-density region ( $\rho[\text{gcm}^{-3}] = 10^{0.5}, 10^{1.5}$  and  $10^{2.5}$ ), the upper right in medium-low density region ( $\rho[\text{gcm}^{-3}] = 10^{3.5}, 10^{4.5}$  and  $10^{5.5}$ ), the lower left in medium-high density region ( $\rho[\text{gcm}^{-3}] = 10^{6.5}, 10^{7.5}$  and  $10^{8.5}$ ) and finally the lower right panel depicts the calculated electron capture rates in high density region ( $\rho[\text{gcm}^{-3}] = 10^{9.5}, 10^{10.5}$  and  $10^{11}$ ). The capture rates are given in logarithmic scale. It can be seen from this figure that in the low density region the capture rates, as a function of temperature, are more or less superimposed on one another. This means that there is no appreciable change in the rates when increasing the density by an order of magnitude. However as one moves from the medium low density region to high density region these rates start to 'peel off' from one another. Orders of magnitude difference in rates are observed (as a function of density) in high density regions. For a given density the rates increase monotonically with increasing temperatures. One also notices that the electron capture rates coincide at  $T_9 = 30\text{K}$  except for the high density region (where  $T_9$  gives the stellar temperature in units of  $10^9\text{K}$ ).

One of the channels for the energy release from the star is the neutrino emission which is mainly from the  $e/e^+$  capture on nucleons and  $e^\pm$  annihilation. Positron capture plays a crucial role in the dynamics of stellar core. They play an indirect role in the reduction of degeneracy pressure of the electrons in the core. Fig.4 shows four panels depicting the calculated positron capture rates at selected temperature and density domain. The upper left panel shows the positron capture rates in low-density region ( $\rho[\text{gcm}^{-3}] = 10^{0.5}, 10^{1.5}$  and  $10^{2.5}$ ), the upper right in medium-low density region ( $\rho[\text{gcm}^{-3}] = 10^{3.5}, 10^{4.5}$  and  $10^{5.5}$ ), the lower left in medium-high density region ( $\rho[\text{gcm}^{-3}] = 10^{6.5}, 10^{7.5}$  and  $10^{8.5}$ ) and finally the lower right panel depicts the calculated positron capture rates in high density region ( $\rho[\text{gcm}^{-3}] = 10^{9.5}, 10^{10.5}$  and  $10^{11}$ ). The positron capture rates are given in logarithmic scales. It is to be noted that the positron capture rates are very slow as compared to electron capture on  $^{24}\text{Mg}$ . The positron capture rates enhance as temperature of the stellar core increases and decrease with increasing stellar density. One should note the order of magnitude differences in positron capture rates as the stellar temperature increases. It can be seen from this figure that in the low density region the positron capture rates, as a function of temperature,

are more or less superimposed on one another (similar to the case of electron capture rates). One also observes that the positron capture rates are almost the same for the densities in the range  $(10 - 10^6)\text{g}/\text{cm}^3$ . However as one moves from the medium high density region to high density region these rates also start to 'peel off' from one another. When the densities increase beyond the above stated range a decline in the positron capture rate starts. For a given density the rates increase monotonically with increasing temperatures.

The reported capture rates on  $^{24}\text{Mg}$  were also compared against two earlier calculations. Fuller, Fowler and Newman [32] (hereafter FFN) compiled the experimental data and calculated electron and positron capture rates (besides other weak-interaction mediated rates) for the nuclei in the mass range  $A = 21-60$  for an extended grid of temperature and density. The GT strength and excitation energies were calculated using a zero-order shell model. For the discrete transitions for which the  $ft$  values were not available FFN took  $\log ft = 5.0$ . Later Oda et al. [6] performed an extensive calculation of stellar weak interaction rates of  $sd$ -shell nuclei in full  $(sd)^n$ -shell model space. They used the effective interaction of Wildenthal [7,33,34] and the available experimental compilations for their calculations.

Fig.5 compares the reported electron capture rates against those of Oda et al. [6] and FFN [32]. It is to be noted that the first two factors in the calculation of capture rates in Eqtn. (2) are similar in all three calculations. Whereas the first factor is a constant, the second factor constitutes the calculation of phase space integrals. The formalism for the calculation of these integrals is similar in all calculations and are dependent only on corresponding stellar temperatures, densities and Fermi energies. The main difference in the three calculations arises because of the third factor (calculation of reduced transition probabilities) which contains in it the in-built nuclear structure effects. In Fig.5  $R_{ec}(QRPA/OHMTS)$  (in the upper panel) is the ratio of the reported electron capture rates to those calculated using shell model by Oda et al [6] whereas  $R_{ec}(QRPA/FFN)$  (in the lower panel) is the ratio of the reported electron capture rates to those calculated by FFN [32]. The shell model electron capture rates are usually in good agreement with the FFN rates. The reported pn-QRPA electron capture rates are enhanced for all values of temperature and density compared to both shell model and FFN results. This is one major difference with the earlier reported capture rates on  $^{24}\text{Mg}$  [14]. For densities around  $\rho[\text{gcm}^{-3}] = 10^3$ , the pn-QRPA rates are enhanced by as much as factor of 14 or more as compared to the corresponding shell model rates. As the density of the stellar matter increases, the enhancement ratio decreases. The pn-QRPA electron capture rates are enhanced by as much as factor of 13 around  $\rho[\text{gcm}^{-3}] = 10^7$  and roughly by a factor of 4 at high density around  $\rho[\text{gcm}^{-3}] = 10^{11}$ . Core-collapse simulators should take note of these enhanced reported electron capture rates. These rates might contribute to some interesting simulation results. A similar comparison for positron capture (pc) rates against previous calculations is shown in the two panels of Fig.6. Here one notes that the reported pn-QRPA positron capture rates are relatively in better agreement with the FFN rates although both FFN and shell model rates are

enhanced. Due to orders of magnitude differences the ratios are plotted on a logarithmic scale in Fig.6. The comparisons are fairly good at high temperatures. It is worth mentioning that the positron capture rates are very small numbers and can change by orders of magnitude by a mere change of 0.5 MeV, or less, in parent or daughter excitation energies and are more reflective of the uncertainties in the calculation of energies.

The calculated electron and positron capture rates on  $^{24}\text{Mg}$  on a fine scale of stellar temperature-density is given in Table 1. The calculated rates are tabulated in logarithmic (to base 10) scale. In the table, -100.000 means that the rate is smaller than  $10^{-100}$ . The first column gives  $\log(\rho Y_e)$  in units of  $gcm^{-3}$ , where  $\rho$  is the baryon density and  $Y_e$  is the ratio of the electron number to the baryon number. Stellar temperatures ( $T_9$ ) are measured in  $10^9$  K. Stated also are the values of the Fermi energy of electrons in units of MeV.  $\lambda^{ec}(\lambda^{pc})$  are the electron(positron) capture rates in units of  $sec^{-1}$  (Eqtn. 3). The ASCII file of Table 1 is also available and can be received from the author upon request.

#### 4. Conclusions

The pn-QRPA theory with separable interaction was used to calculate the electron and positron capture rates on  $^{24}\text{Mg}$  on a much detailed temperature-density grid point suitable for simulation purposes. Deformation parameter, which is believed to be one of the important parameters of pn-QRPA calculations, was taken from the experimental compilation to further increase the reliability of the calculations. The reported electron capture rates are enhanced, by as much as a factor of 12, compared to the shell model results of Oda and collaborators [6].

There exists a wide variety of discrepant results in the supernova simulations of O+Ne+Mg cores including prompt explosions, delayed explosions and no explosions. Fryer et al. [35] and Kitaura et al. [9] pointed that a possible explanation to these varying results could be explained by the different nuclear equation of states employed in the simulations and the treatment of capture rates on a large variety of nuclei both in nuclear statistical equilibrium (NSE) and in the non-NSE regime. Recent simulations of O+Ne+Mg cores by Gutiérrez et al. [8] and Kitaura et al. [9] employ the shell model capture rates of Oda et al. [6] and Takahara et al. [10], respectively. The spherical core collapse simulations do not explode partly because of the reduced electron capture rates in the non-NSE regime slowing the collapse and resulting in a large shock radius.

It can be expected that a parameter-free multi-dimensional model, with neutrino transport included consistently throughout the entire mass, including a complete treatment of multidimensional convection and burning phases might lead to a better understanding of the phenomena of supernova explosions. Incorporation of the reported (enhanced) capture rates might point toward still lower values of  $Y_e$  and lower entropy in the stellar core and might give some interesting results for simulators transforming a collapse into an explosion.



## Acknowledgments

The author would like to acknowledge the local hospitality provided by the Abdus Salam ICTP, Trieste, where part of this project was completed.

## References

- [1] Arnett D 1996 *Supernovae and Nucleosynthesis* (New Jersey: Princeton University Press)
- [2] Dessart L, Burrows A, Livne E and Ott C D 2007 *Astrophys. J.* **669** 585
- [3] Hillebrandt W 1978 *Space Sci. Rev.* **21** 639
- [4] Sumiyoshi K, Terasawa M, Mathews G J, Kajino T, Yamada S and Suzuki H 2001 *Astrophys. J.* **562** 880
- [5] Wanaajo S, Tamamura M, Naoki I, Nomoto K, Ishimaru Y, Beers T C and Nozawa S 2003 *Astrophys. J.* **593** 968
- [6] Oda T, Hino M, Muto K, Takahara M and Sato K 1994 *At. Data Nucl. Data Tables* **56** 231
- [7] Wildenthal B H 1984 in *Progress in Particle and Nuclear Physics, vol 11, pg 5*, ed D H Wilkinson (Oxford: Pergamon)
- [8] Gutiérrez J, Canal R and García-Berro E 2005 *Astron. and Astrophys.* **435** 231
- [9] Kitaura F S, Janka H-Th and Hillebrandt W 2006 *Astron. and Astrophys.* **450** 345
- [10] Takahara M, Hino M, Oda T, Muto K, Wolters A A, Glaudemans P W M and Sato K 1989 *Nucl. Phys.* **A504** 167
- [11] Nabi J-Un 1999 *PhD Thesis*, (Germany: Heidelberg University)
- [12] Nabi J-Un and Klapdor-Kleingrothaus H V 1999 *At. Data Nucl. Data Tables* **71** 149–345
- [13] Nabi J-Un and Klapdor-Kleingrothaus H V 2004 *At. Data Nucl. Data Tables* **88** 237–476
- [14] Nabi J-Un and Rahman M-Ur 2007 *Phys. Rev. C* **75** 035803
- [15] Nabi J-Un and Rahman M-Ur 2005 *Phys. Lett.* **B612** 190–6
- [16] Nabi J-Un and Sajjad M 2007 *Phys. Rev. C* **76** 055803
- [17] Nabi J-Un, Sajjad M and Rahman M-Ur 2007 *Acta Phys. Pol. B* **38** 3203–23
- [18] Stetcu I and Johnson C W 2004 *Phys. Rev. C* **69** 024311
- [19] Raman S, Malarkey C H, Milner W T, Nestor, Jr C W and Stelson P H 1987 *At. Data Nucl. Data Tables* **36** 1–196
- [20] Nilsson S G 1955 *Mat. Fys. Medd. Dan. Vid. Selsk* **29** 16
- [21] Hirsch M, Staudt A, Muto K and Klapdor-Kleingrothaus H V 1991 *Nucl. Phys.* **A535** 62
- [22] Audi G, Wapstra A H and Thibault C 2003 *Nucl. Phys.* **A729** 337
- [23] Yost G P *et al.* (Particle Data Group) 1988 *Phys. Lett.* **B204** 1
- [24] Rodin V, Faessler A, Simkovic F and Vogel P 2006 *Czech. J. Phys.* **56** 495
- [25] Nabi J-Un, Rahman M-Ur and Sajjad M 2007 *Braz. J. Phys.* **37** 1238–45
- [26] Martinez-Pinedo G, Poves A, Caurier E and Zuker A P 1996 *Phys. Rev. C* **53** R2602
- [27] Rakers S, Bäumer C, Frekers D, Schmidt R, van den Berg A M, Hannen V M, Harakeh M N, de Huu M A, Wörtche H J, De Frenne D, Hagemann M, Heyse J, Jacobs E and Fujita Y 2002 *Phys. Rev. C* **65** 044323
- [28] Möller P and Nix J R 1981 *At. Data Nucl. Data Tables* **26** 165
- [29] Hirsch M, Staudt A, Muto K and Klapdor-Kleingrothaus H V 1993 *At. Data Nucl. Data Tables* **53** 165–93
- [30] Brown B A and Wildenthal B H 1983 *Phys. Rev. C* **27** 1296
- [31] Wildenthal B H 1984 *Prog. Part. Nucl. Phys.* **11** 5
- [32] Fuller G M, Fowler W A and Newman M J 1980 *Astrophys. J. Suppl.* **42** 447; Fuller G M, Fowler W A and Newman M J 1982 *Astrophys. J. Suppl.* **48** 279; Fuller G M, Fowler W A and Newman M J 1982 *Astrophys. J.* **252** 715; Fuller G M, Fowler W A and Newman M J 1985 *Astrophys. J.* **293** 1

- [33] Brown B A, Chung W and Wildenthal B H 1978 *Phys. Rev. Lett.* **40** 1631
- [34] Brown B A and Wildenthal B H 1985 *At. Data Nucl. Data Tables* **33** 347
- [35] Fryer C L, Benz W, Herant M and Colgate S 1999 *Astrophys. J.* **516** 892

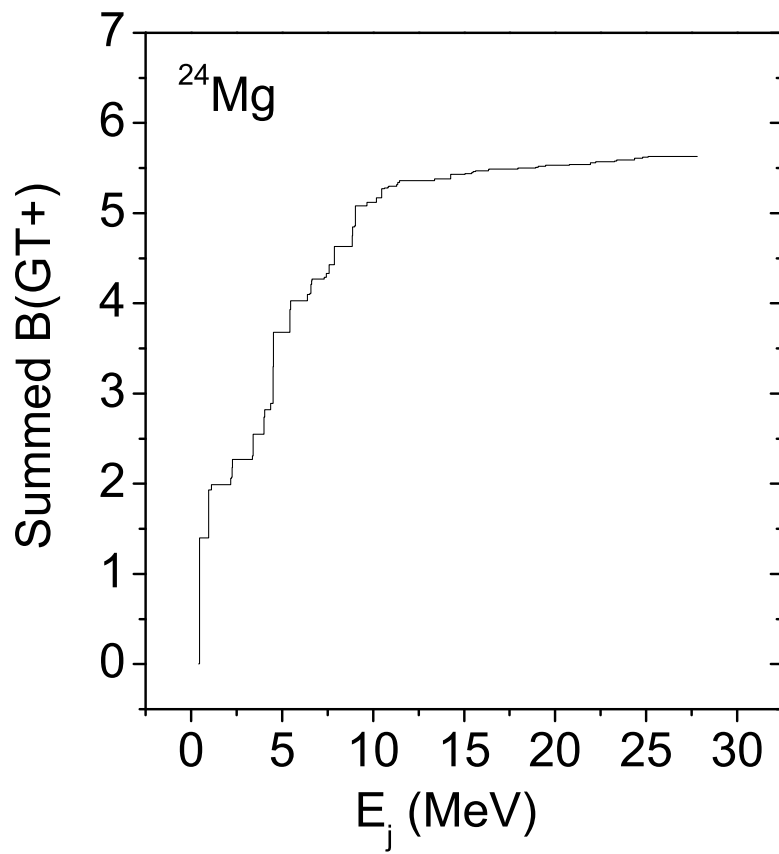


**Figure 1.** Cumulative sum of the unquenched  $B(\text{GT}^+)$  values.  $E_j$  represents the daughter excitation energies in  $^{24}\text{Na}$ .

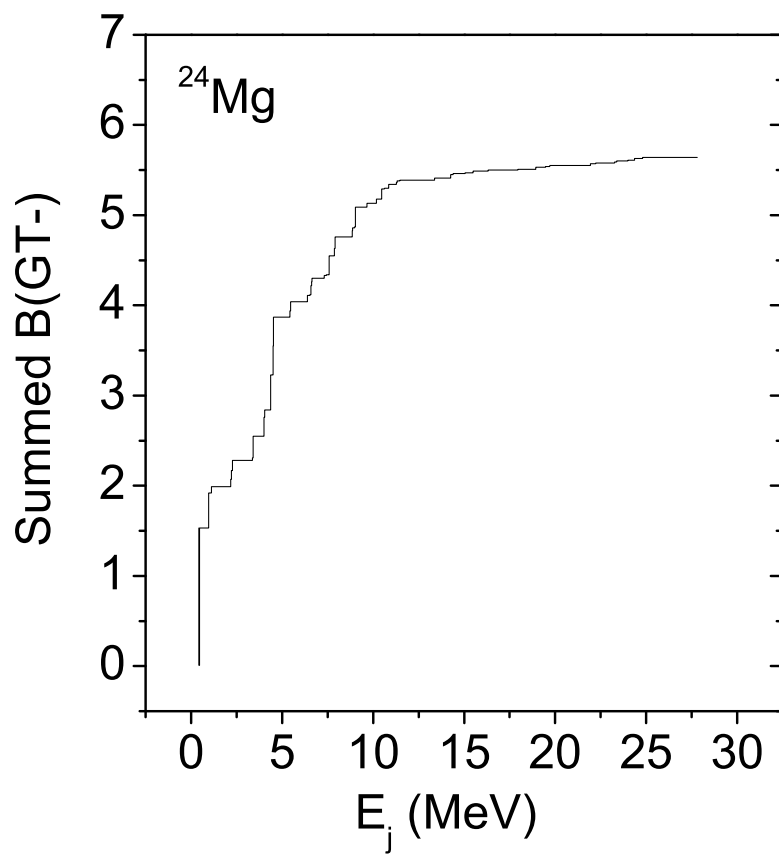


**Figure 2.** Cumulative sum of the unquenched  $B(\text{GT}^-)$  values.  $E_j$  represents the daughter excitation energies in  $^{24}\text{Al}$ .

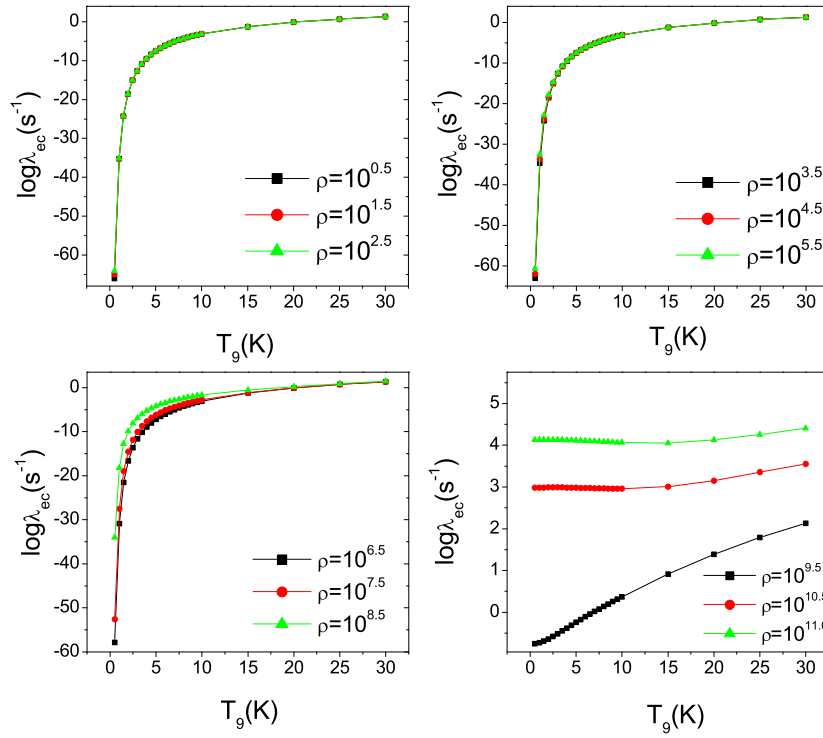


**Figure 3.** (Color online) Electron capture rates on  $^{24}\text{Mg}$ , as function of temperature, for different selected densities. Densities are in units of  $\text{g cm}^{-3}$ . Temperatures are measured in  $10^9 \text{ K}$  and  $\log \lambda_{ec}$  represents the log of electron capture rates in units of  $\text{sec}^{-1}$ .

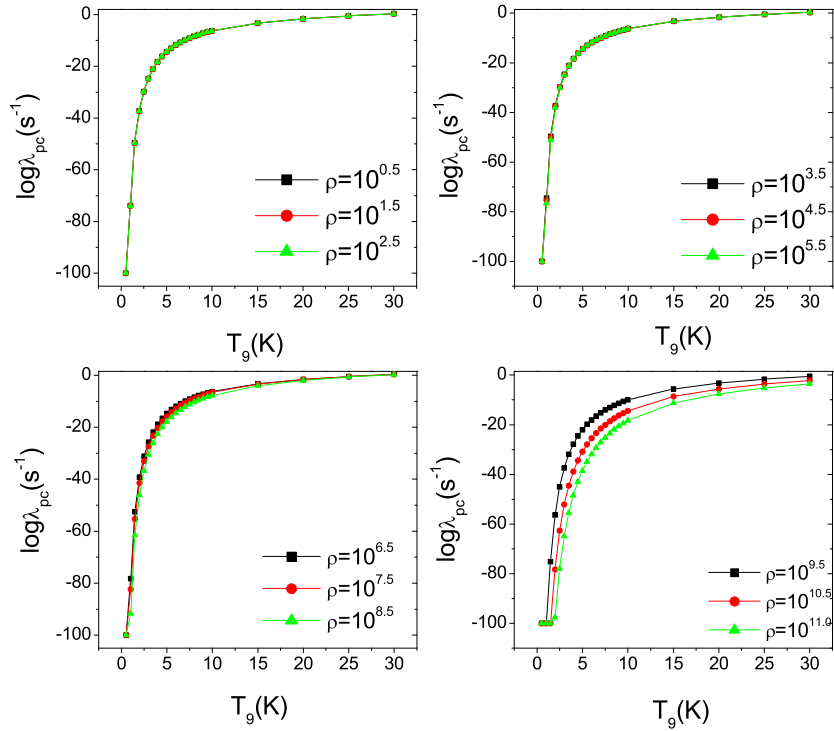


**Figure 4.** (Color online) Positron capture rates on  $^{24}\text{Mg}$ , as function of temperature, for different selected densities. Densities are in units of  $\text{g cm}^{-3}$ . Temperatures are measured in  $10^9$  K and  $\log \lambda_{pc}$  represents the log of positron capture rates in units of  $\text{sec}^{-1}$ .

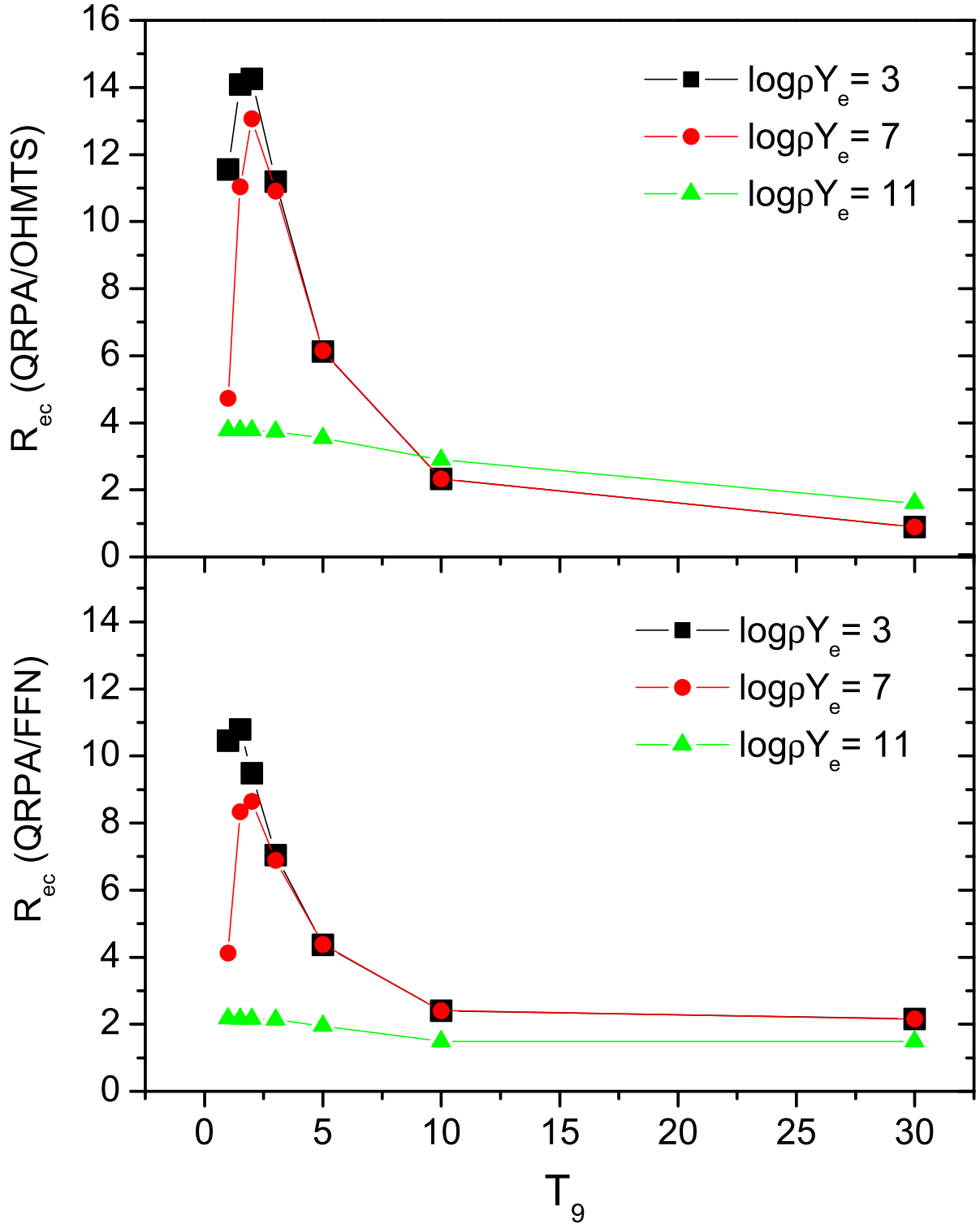


**Figure 5.** (Color online) Ratios of reported electron capture rates to those calculated using shell model [6] (upper panel) and FFN [32] (lower panel) on  $^{24}\text{Mg}$  as function of stellar temperatures and densities.  $T_9$  measures the stellar temperature in units of  $10^9\text{K}$

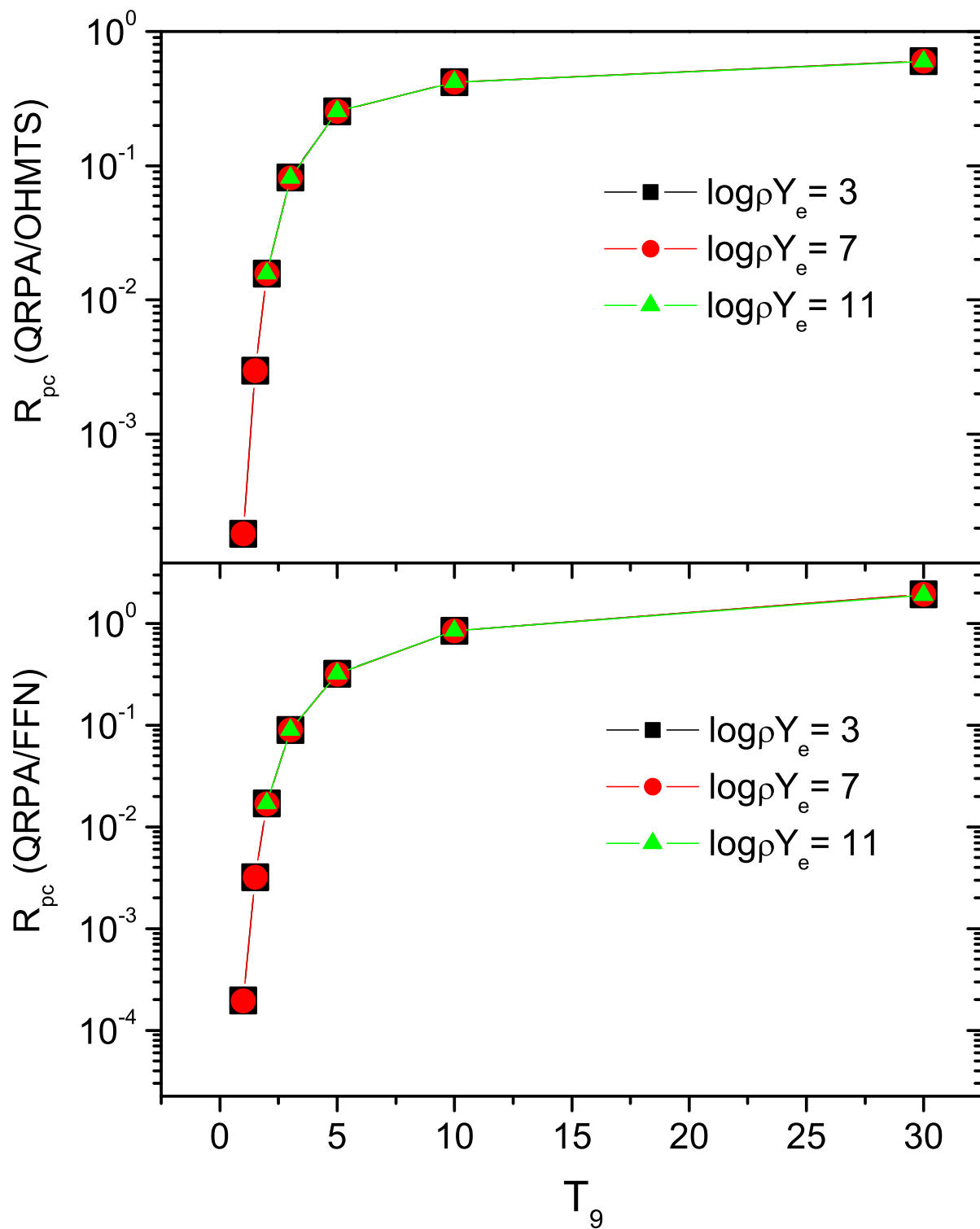


Figure 6. (Color online) Same as Fig. 5 but for positron capture (pc) rates.



**Table 1:** Calculated electron and positron capture rates on  $^{24}\text{Mg}$  for different selected densities and temperatures in stellar matter.  $\log(\rho Y_e)$  has units of  $gcm^{-3}$ , where  $\rho$  is the baryon density and  $Y_e$  is the ratio of the electron number to the baryon number. Temperatures ( $T_9$ ) are measured in  $10^9$  K.  $E_f$  is the total Fermi energy of electrons including the rest mass(MeV).  $\lambda^{ec}(\lambda^{pc})$  are the electron(positron) capture rates ( $sec^{-1}$ ). The calculated rates are tabulated in logarithmic (to base 10) scale. In the table, -100.000 means that the rate is smaller than  $10^{-100}$ .

$\log\rho Y_e$	$T_9$	$E_f$	$\lambda^{ec}$	$\lambda^{pc}$	$\log\rho Y_e$	$T_9$	$E_f$	$\lambda^{ec}$	$\lambda^{pc}$	$\log\rho Y_e$	$T_9$	$E_f$	$\lambda^{ec}$	$\lambda^{pc}$
0.5	0.5	0.065	-66.044	-100	1	8.5	0	-3.952	-7.796	2	4.5	0	-8.4	-16.178
0.5	1	0	-35.225	-73.878	1	9	0	-3.64	-7.247	2	5	0	-7.512	-14.438
0.5	1.5	0	-24.272	-49.645	1	9.5	0	-3.355	-6.75	2	5.5	0	-6.768	-13.002
0.5	2	0	-18.568	-37.28	1	10	0	-3.093	-6.299	2	6	0	-6.133	-11.795
0.5	2.5	0	-15.038	-29.776	1	15	0	-1.249	-3.296	2	6.5	0	-5.584	-10.765
0.5	3	0	-12.619	-24.726	1	20	0	-0.113	-1.621	2	7	0	-5.103	-9.875
0.5	3.5	0	-10.848	-21.088	1	25	0	0.707	-0.5	2	7.5	0	-4.677	-9.096
0.5	4	0	-9.486	-18.337	1	30	0	1.343	0.327	2	8	0	-4.296	-8.408
0.5	4.5	0	-8.401	-16.179	1.5	0.5	0.162	-65.065	-100	2	8.5	0	-3.952	-7.796
0.5	5	0	-7.512	-14.439	1.5	1	0.002	-35.218	-73.885	2	9	0	-3.64	-7.247
0.5	5.5	0	-6.768	-13.003	1.5	1.5	0	-24.272	-49.645	2	9.5	0	-3.355	-6.75
0.5	6	0	-6.134	-11.796	1.5	2	0	-18.568	-37.279	2	10	0	-3.092	-6.299
0.5	6.5	0	-5.585	-10.766	1.5	2.5	0	-15.037	-29.776	2	15	0	-1.249	-3.296
0.5	7	0	-5.104	-9.876	1.5	3	0	-12.619	-24.726	2	20	0	-0.112	-1.62
0.5	7.5	0	-4.678	-9.097	1.5	3.5	0	-10.847	-21.088	2	25	0	0.707	-0.499
0.5	8	0	-4.297	-8.409	1.5	4	0	-9.485	-18.336	2	30	0	1.343	0.328
0.5	8.5	0	-3.953	-7.797	1.5	4.5	0	-8.4	-16.178	2.5	0.5	0.261	-64.065	-100
0.5	9	0	-3.641	-7.247	1.5	5	0	-7.512	-14.438	2.5	1	0.015	-35.149	-73.953
0.5	9.5	0	-3.356	-6.751	1.5	5.5	0	-6.768	-13.002	2.5	1.5	0.002	-24.267	-49.649
0.5	10	0	-3.093	-6.3	1.5	6	0	-6.133	-11.795	2.5	2	0	-18.567	-37.28
0.5	15	0	-1.25	-3.297	1.5	6.5	0	-5.584	-10.766	2.5	2.5	0	-15.037	-29.776
0.5	20	0	-0.114	-1.622	1.5	7	0	-5.103	-9.875	2.5	3	0	-12.619	-24.726
0.5	25	0	0.705	-0.501	1.5	7.5	0	-4.677	-9.096	2.5	3.5	0	-10.847	-21.088
0.5	30	0	1.342	0.326	1.5	8	0	-4.296	-8.409	2.5	4	0	-9.485	-18.336
1	0.5	0.113	-65.563	-100	1.5	8.5	0	-3.952	-7.796	2.5	4.5	0	-8.4	-16.178
1	1	0	-35.223	-73.88	1.5	9	0	-3.64	-7.247	2.5	5	0	-7.512	-14.438
1	1.5	0	-24.272	-49.645	1.5	9.5	0	-3.355	-6.75	2.5	5.5	0	-6.768	-13.002
1	2	0	-18.568	-37.279	1.5	10	0	-3.092	-6.299	2.5	6	0	-6.133	-11.795
1	2.5	0	-15.037	-29.776	1.5	15	0	-1.249	-3.296	2.5	6.5	0	-5.584	-10.765
1	3	0	-12.619	-24.726	1.5	20	0	-0.112	-1.62	2.5	7	0	-5.103	-9.875
1	3.5	0	-10.847	-21.088	1.5	25	0	0.707	-0.499	2.5	7.5	0	-4.677	-9.096
1	4	0	-9.485	-18.336	1.5	30	0	1.343	0.328	2.5	8	0	-4.296	-8.408
1	4.5	0	-8.4	-16.179	2	0.5	0.212	-64.565	-100	2.5	8.5	0	-3.952	-7.796
1	5	0	-7.512	-14.438	2	1	0.005	-35.201	-73.901	2.5	9	0	-3.64	-7.247
1	5.5	0	-6.768	-13.002	2	1.5	0	-24.27	-49.646	2.5	9.5	0	-3.355	-6.75
1	6	0	-6.133	-11.796	2	2	0	-18.568	-37.28	2.5	10	0	-3.092	-6.299
1	6.5	0	-5.584	-10.766	2	2.5	0	-15.037	-29.776	2.5	15	0	-1.249	-3.296
1	7	0	-5.103	-9.875	2	3	0	-12.619	-24.726	2.5	20	0	-0.112	-1.62
1	7.5	0	-4.677	-9.096	2	3.5	0	-10.847	-21.088	2.5	25	0	0.707	-0.499
1	8	0	-4.296	-8.409	2	4	0	-9.485	-18.336	2.5	30	0	1.343	0.328

$\log\rho Y_e$	$T_9$	$E_f$	$\lambda^{ec}$	$\lambda^{pc}$	$\log\rho Y_e$	$T_9$	$E_f$	$\lambda^{ec}$	$\lambda^{pc}$	$\log\rho Y_e$	$T_9$	$E_f$	$\lambda^{ec}$	$\lambda^{pc}$
3	0.5	0.311	-63.564	-100	4	0.5	0.411	-62.552	-100	5	0.5	0.522	-61.433	-100
3	1	0.046	-34.995	-74.107	4	1	0.209	-34.173	-74.929	5	1	0.413	-33.142	-75.961
3	1.5	0.005	-24.256	-49.661	4	1.5	0.047	-24.114	-49.802	5	1.5	0.265	-23.381	-50.536
3	2	0.001	-18.565	-37.283	4	2	0.014	-18.533	-37.314	5	2	0.128	-18.244	-37.603
3	2.5	0.001	-15.036	-29.777	4	2.5	0.006	-15.025	-29.788	5	2.5	0.062	-14.912	-29.901
3	3	0	-12.618	-24.726	4	3	0.004	-12.613	-24.732	5	3	0.035	-12.559	-24.785
3	3.5	0	-10.847	-21.088	4	3.5	0.002	-10.844	-21.091	5	3.5	0.023	-10.814	-21.12
3	4	0	-9.485	-18.336	4	4	0.002	-9.483	-18.338	5	4	0.016	-9.465	-18.356
3	4.5	0	-8.4	-16.179	4	4.5	0.001	-8.399	-16.18	5	4.5	0.012	-8.387	-16.192
3	5	0	-7.512	-14.438	4	5	0.001	-7.511	-14.439	5	5	0.009	-7.502	-14.447
3	5.5	0	-6.767	-13.002	4	5.5	0.001	-6.767	-13.003	5	5.5	0.007	-6.761	-13.009
3	6	0	-6.133	-11.795	4	6	0.001	-6.133	-11.796	5	6	0.006	-6.128	-11.8
3	6.5	0	-5.584	-10.765	4	6.5	0.001	-5.584	-10.766	5	6.5	0.005	-5.58	-10.769
3	7	0	-5.103	-9.875	4	7	0	-5.103	-9.875	5	7	0.004	-5.1	-9.878
3	7.5	0	-4.677	-9.096	4	7.5	0	-4.677	-9.096	5	7.5	0.004	-4.674	-9.099
3	8	0	-4.296	-8.408	4	8	0	-4.296	-8.409	5	8	0.003	-4.294	-8.41
3	8.5	0	-3.952	-7.796	4	8.5	0	-3.952	-7.796	5	8.5	0.003	-3.95	-7.798
3	9	0	-3.64	-7.246	4	9	0	-3.64	-7.247	5	9	0.002	-3.639	-7.248
3	9.5	0	-3.355	-6.75	4	9.5	0	-3.355	-6.75	5	9.5	0.002	-3.353	-6.751
3	10	0	-3.092	-6.299	4	10	0	-3.092	-6.299	5	10	0.002	-3.091	-6.3
3	15	0	-1.248	-3.296	4	15	0	-1.248	-3.296	5	15	0.001	-1.248	-3.296
3	20	0	-0.112	-1.62	4	20	0	-0.112	-1.62	5	20	0	-0.112	-1.62
3	25	0	0.707	-0.499	4	25	0	0.707	-0.499	5	25	0	0.707	-0.499
3	30	0	1.344	0.328	4	30	0	1.344	0.328	5	30	0	1.344	0.328
3.5	0.5	0.361	-63.061	-100	4.5	0.5	0.464	-62.023	-100	5.5	0.5	0.598	-60.675	-100
3.5	1	0.115	-34.647	-74.455	4.5	1	0.309	-33.667	-75.435	5.5	1	0.528	-32.563	-76.54
3.5	1.5	0.015	-24.221	-49.695	4.5	1.5	0.13	-23.836	-50.08	5.5	1.5	0.423	-22.852	-51.066
3.5	2	0.004	-18.557	-37.29	4.5	2	0.044	-18.458	-37.389	5.5	2	0.295	-17.824	-38.024
3.5	2.5	0.002	-15.033	-29.78	4.5	2.5	0.02	-14.997	-29.816	5.5	2.5	0.18	-14.674	-30.139
3.5	3	0.001	-12.617	-24.728	4.5	3	0.011	-12.6	-24.745	5.5	3	0.11	-12.435	-24.91
3.5	3.5	0.001	-10.846	-21.089	4.5	3.5	0.007	-10.837	-21.098	5.5	3.5	0.072	-10.744	-21.191
3.5	4	0.001	-9.485	-18.337	4.5	4	0.005	-9.479	-18.342	5.5	4	0.05	-9.422	-18.4
3.5	4.5	0	-8.4	-16.179	4.5	4.5	0.004	-8.396	-16.183	5.5	4.5	0.038	-8.358	-16.22
3.5	5	0	-7.511	-14.438	4.5	5	0.003	-7.509	-14.441	5.5	5	0.029	-7.482	-14.467
3.5	5.5	0	-6.767	-13.002	4.5	5.5	0.002	-6.765	-13.004	5.5	5.5	0.023	-6.746	-13.023
3.5	6	0	-6.133	-11.796	4.5	6	0.002	-6.132	-11.797	5.5	6	0.019	-6.117	-11.811
3.5	6.5	0	-5.584	-10.766	4.5	6.5	0.002	-5.583	-10.767	5.5	6.5	0.016	-5.572	-10.778
3.5	7	0	-5.103	-9.875	4.5	7	0.001	-5.102	-9.876	5.5	7	0.013	-5.093	-9.885
3.5	7.5	0	-4.677	-9.096	4.5	7.5	0.001	-4.676	-9.097	5.5	7.5	0.012	-4.669	-9.104
3.5	8	0	-4.296	-8.408	4.5	8	0.001	-4.295	-8.409	5.5	8	0.01	-4.289	-8.415
3.5	8.5	0	-3.952	-7.796	4.5	8.5	0.001	-3.952	-7.797	5.5	8.5	0.009	-3.947	-7.801
3.5	9	0	-3.64	-7.247	4.5	9	0.001	-3.64	-7.247	5.5	9	0.008	-3.636	-7.251
3.5	9.5	0	-3.355	-6.75	4.5	9.5	0.001	-3.354	-6.75	5.5	9.5	0.007	-3.351	-6.754
3.5	10	0	-3.092	-6.299	4.5	10	0.001	-3.092	-6.299	5.5	10	0.006	-3.089	-6.302
3.5	15	0	-1.248	-3.296	4.5	15	0	-1.248	-3.296	5.5	15	0.003	-1.248	-3.296
3.5	20	0	-0.112	-1.62	4.5	20	0	-0.112	-1.62	5.5	20	0.001	-0.112	-1.621
3.5	25	0	0.707	-0.499	4.5	25	0	0.707	-0.499	5.5	25	0.001	0.707	-0.499
3.5	30	0	1.344	0.328	4.5	30	0	1.344	0.328	5.5	30	0.001	1.344	0.328

$\log\rho Y_e$	$T_9$	$E_f$	$\lambda^{ec}$	$\lambda^{pc}$	$\log\rho Y_e$	$T_9$	$E_f$	$\lambda^{ec}$	$\lambda^{pc}$	$\log\rho Y_e$	$T_9$	$E_f$	$\lambda^{ec}$	$\lambda^{pc}$
6	0.5	0.713	-59.518	-100	7	0.5	1.217	-56.24	-100	8	0.5	2.444	-45.14	-100
6	1	0.672	-31.846	-77.264	7	1	1.2	-29.578	-79.927	8	1	2.437	-23.824	-86.158
6	1.5	0.604	-22.248	-51.673	7	1.5	1.173	-20.447	-53.584	8	1.5	2.424	-16.495	-57.788
6	2	0.512	-17.279	-38.571	7	2	1.133	-15.756	-40.136	8	2	2.406	-12.716	-43.342
6	2.5	0.405	-14.223	-30.592	7	2.5	1.083	-12.877	-31.959	8	2.5	2.383	-10.375	-34.58
6	3	0.299	-12.117	-25.228	7	3	1.021	-10.916	-26.442	8	3	2.355	-8.766	-28.682
6	3.5	0.214	-10.539	-21.396	7	3.5	0.95	-9.488	-22.456	8	3.5	2.322	-7.582	-24.431
6	4	0.156	-9.289	-18.532	7	4	0.871	-8.395	-19.433	8	4	2.283	-6.669	-21.213
6	4.5	0.117	-8.269	-16.31	7	4.5	0.785	-7.525	-17.058	8	4.5	2.24	-5.94	-18.687
6	5	0.091	-7.42	-14.53	7	5	0.698	-6.811	-15.142	8	5	2.192	-5.342	-16.648
6	5.5	0.073	-6.701	-13.069	7	5.5	0.613	-6.209	-13.564	8	5.5	2.139	-4.841	-14.962
6	6	0.06	-6.083	-11.846	7	6	0.534	-5.686	-12.244	8	6	2.081	-4.414	-13.543
6	6.5	0.05	-5.546	-10.804	7	6.5	0.465	-5.226	-11.126	8	6.5	2.019	-4.043	-12.331
6	7	0.042	-5.073	-9.905	7	7	0.404	-4.814	-10.166	8	7	1.952	-3.719	-11.28
6	7.5	0.036	-4.652	-9.121	7	7.5	0.353	-4.441	-9.333	8	7.5	1.882	-3.431	-10.361
6	8	0.032	-4.276	-8.428	7	8	0.31	-4.101	-8.604	8	8	1.808	-3.173	-9.548
6	8.5	0.028	-3.936	-7.812	7	8.5	0.274	-3.79	-7.959	8	8.5	1.732	-2.94	-8.823
6	9	0.025	-3.626	-7.26	7	9	0.244	-3.504	-7.383	8	9	1.653	-2.727	-8.172
6	9.5	0.022	-3.343	-6.762	7	9.5	0.218	-3.24	-6.866	8	9.5	1.574	-2.531	-7.585
6	10	0.02	-3.082	-6.309	7	10	0.196	-2.994	-6.398	8	10	1.493	-2.35	-7.051
6	15	0.009	-1.246	-3.298	7	15	0.085	-1.22	-3.324	8	15	0.817	-0.978	-3.57
6	20	0.005	-0.111	-1.621	7	20	0.047	-0.1	-1.632	8	20	0.47	0.004	-1.738
6	25	0.003	0.708	-0.5	7	25	0.03	0.713	-0.505	8	25	0.301	0.767	-0.56
6	30	0.002	1.344	0.328	7	30	0.021	1.347	0.324	8	30	0.209	1.378	0.293
6.5	0.5	0.905	-57.811	-100	7.5	0.5	1.705	-52.593	-100	8.5	0.5	3.547	-34.019	-100
6.5	1	0.88	-30.857	-78.31	7.5	1	1.693	-27.533	-82.412	8.5	1	3.542	-18.252	-91.73
6.5	1.5	0.837	-21.483	-52.456	7.5	1.5	1.675	-18.944	-55.271	8.5	1.5	3.534	-12.769	-61.517
6.5	2	0.777	-16.621	-39.237	7.5	2	1.648	-14.55	-41.433	8.5	2	3.521	-9.916	-46.153
6.5	2.5	0.701	-13.63	-31.189	7.5	2.5	1.614	-11.857	-33.03	8.5	2.5	3.506	-8.134	-36.843
6.5	3	0.612	-11.594	-25.754	7.5	3	1.573	-10.022	-27.368	8.5	3	3.487	-6.898	-30.583
6.5	3.5	0.517	-10.105	-21.832	7.5	3.5	1.524	-8.683	-23.282	8.5	3.5	3.464	-5.978	-26.076
6.5	4	0.424	-8.953	-18.87	7.5	4	1.468	-7.658	-20.186	8.5	4	3.438	-5.259	-22.668
6.5	4.5	0.343	-8.018	-16.562	7.5	4.5	1.405	-6.843	-17.752	8.5	4.5	3.408	-4.677	-19.996
6.5	5	0.277	-7.233	-14.717	7.5	5	1.336	-6.178	-15.785	8.5	5	3.375	-4.194	-17.84
6.5	5.5	0.226	-6.561	-13.209	7.5	5.5	1.262	-5.622	-14.158	8.5	5.5	3.339	-3.784	-16.062
6.5	6	0.187	-5.977	-11.952	7.5	6	1.183	-5.148	-12.789	8.5	6	3.299	-3.431	-14.566
6.5	6.5	0.157	-5.463	-10.887	7.5	6.5	1.101	-4.738	-11.619	8.5	6.5	3.256	-3.122	-13.29
6.5	7	0.134	-5.007	-9.971	7.5	7	1.018	-4.376	-10.608	8.5	7	3.209	-2.849	-12.185
6.5	7.5	0.115	-4.6	-9.173	7.5	7.5	0.937	-4.053	-9.725	8.5	7.5	3.159	-2.606	-11.219
6.5	8	0.1	-4.233	-8.471	7.5	8	0.858	-3.76	-8.949	8.5	8	3.106	-2.386	-10.365
6.5	8.5	0.088	-3.9	-7.848	7.5	8.5	0.783	-3.492	-8.26	8	5 8.5	3.05	-2.187	-9.604
6.5	9	0.078	-3.597	-7.29	7.5	9	0.714	-3.244	-7.646	8.5	9	2.99	-2.005	-8.921
6.5	9.5	0.069	-3.318	-6.787	7.5	9.5	0.651	-3.012	-7.095	8.5	9.5	2.928	-1.838	-8.303
6.5	10	0.062	-3.061	-6.33	7.5	10	0.593	-2.796	-6.598	8.5	10	2.863	-1.683	-7.741
6.5	15	0.027	-1.239	-3.305	7.5	15	0.268	-1.159	-3.386	8.5	15	2.109	-0.554	-4.004
6.5	20	0.015	-0.109	-1.624	7.5	20	0.15	-0.075	-1.658	8.5	20	1.402	0.235	-1.973
6.5	25	0.01	0.709	-0.501	7.5	25	0.095	0.726	-0.518	8.5	25	0.936	0.892	-0.687
6.5	30	0.007	1.345	0.327	7.5	30	0.066	1.355	0.317	8.5	30	0.656	1.452	0.218

$\log\rho Y_e$	$T_9$	$E_f$	$\lambda^{ec}$	$\lambda^{pc}$	$\log\rho Y_e$	$T_9$	$E_f$	$\lambda^{ec}$	$\lambda^{pc}$	$\log\rho Y_e$	$T_9$	$E_f$	$\lambda^{ec}$	$\lambda^{pc}$
9	0.5	5.179	-17.57	-100	9.5	8.5	7.351	0.199	-12.155	10.5	4.5	16.28	2.986	-34.412
9	1	5.176	-10.019	-99.963	9.5	9	7.323	0.258	-11.347	10.5	5	16.273	2.983	-30.841
9	1.5	5.17	-7.271	-67.015	9.5	9.5	7.293	0.315	-10.619	10.5	5.5	16.265	2.98	-27.907
9	2	5.162	-5.783	-50.286	9.5	10	7.261	0.373	-9.958	10.5	6	16.256	2.977	-25.451
9	2.5	5.151	-4.819	-40.16	9.5	15	6.86	0.917	-5.6	10.5	6.5	16.247	2.974	-23.363
9	3	5.138	-4.128	-33.357	9.5	20	6.307	1.392	-3.209	10.5	7	16.237	2.971	-21.565
9	3.5	5.122	-3.599	-28.464	9.5	25	5.624	1.792	-1.632	10.5	7.5	16.226	2.968	-20
9	4	5.105	-3.175	-24.768	9.5	30	4.859	2.131	-0.487	10.5	8	16.214	2.966	-18.623
9	4.5	5.085	-2.824	-21.873	10	0.5	11.118	1.613	-100	10.5	8.5	16.202	2.964	-17.403
9	5	5.062	-2.525	-19.54	10	1	11.116	1.615	-100	10.5	9	16.189	2.962	-16.312
9	5.5	5.037	-2.266	-17.618	10	1.5	11.113	1.618	-86.985	10.5	9.5	16.175	2.961	-15.331
9	6	5.01	-2.037	-16.004	10	2	11.11	1.622	-65.275	10.5	10	16.16	2.96	-14.444
9	6.5	4.98	-1.833	-14.627	10	2.5	11.105	1.626	-52.162	10.5	15	15.973	3.005	-8.662
9	7	4.948	-1.648	-13.438	10	3	11.099	1.631	-43.371	10.5	20	15.711	3.152	-5.579
9	7.5	4.914	-1.479	-12.398	10	3.5	11.091	1.635	-37.059	10.5	25	15.375	3.353	-3.598
9	8	4.878	-1.324	-11.481	10	4	11.083	1.64	-32.301	10.5	30	14.965	3.555	-2.185
9	8.5	4.839	-1.181	-10.665	10	4.5	11.074	1.645	-28.581	11	0.5	23.934	4.131	-100
9	9	4.797	-1.048	-9.933	10	5	11.063	1.649	-25.59	11	1	23.933	4.131	-100
9	9.5	4.754	-0.923	-9.272	10	5.5	11.052	1.654	-23.13	11	1.5	23.932	4.131	-100
9	10	4.708	-0.806	-8.671	10	6	11.039	1.66	-21.068	11	2	23.93	4.131	-97.582
9	15	4.131	0.091	-4.683	10	6.5	11.025	1.666	-19.314	11	2.5	23.928	4.131	-78.013
9	20	3.39	0.717	-2.474	10	7	11.011	1.672	-17.802	11	3	23.925	4.13	-64.919
9	25	2.621	1.222	-1.027	10	7.5	10.995	1.68	-16.484	11	3.5	23.922	4.128	-55.534
9	30	1.973	1.668	-0.003	10	8	10.978	1.688	-15.324	11	4	23.918	4.126	-48.472
9.5	0.5	7.583	-0.75	-100	10	8.5	10.959	1.697	-14.294	11	4.5	23.913	4.122	-42.961
9.5	1	7.581	-0.726	-100	10	9	10.94	1.707	-13.373	11	5	23.908	4.118	-38.538
9.5	1.5	7.577	-0.688	-75.102	10	9.5	10.92	1.718	-12.543	11	5.5	23.903	4.113	-34.906
9.5	2	7.571	-0.638	-56.359	10	10	10.898	1.731	-11.792	11	6	23.897	4.107	-31.869
9.5	2.5	7.564	-0.579	-45.024	10	15	10.624	1.927	-6.865	11	6.5	23.891	4.102	-29.29
9.5	3	7.555	-0.514	-37.418	10	20	10.241	2.216	-4.2	11	7	23.884	4.096	-27.071
9.5	3.5	7.545	-0.447	-31.952	10	25	9.751	2.514	-2.464	11	7.5	23.877	4.091	-25.141
9.5	4	7.532	-0.378	-27.827	10	30	9.163	2.783	-1.21	11	8	23.869	4.085	-23.445
9.5	4.5	7.519	-0.308	-24.599	10.5	0.5	16.31	2.987	-100	11	8.5	23.86	4.08	-21.944
9.5	5	7.503	-0.24	-22.001	10.5	1	16.309	2.987	-100	11	9	23.851	4.075	-20.603
9.5	5.5	7.486	-0.173	-19.862	10.5	1.5	16.307	2.988	-100	11	9.5	23.842	4.07	-19.399
9.5	6	7.468	-0.108	-18.068	10.5	2	16.304	2.989	-78.366	11	10	23.832	4.066	-18.31
9.5	6.5	7.448	-0.044	-16.54	10.5	2.5	16.301	2.989	-62.638	11	15	23.704	4.055	-11.26
9.5	7	7.426	0.018	-15.221	10.5	3	16.297	2.99	-52.104	11	20	23.526	4.127	-7.548
9.5	7.5	7.403	0.079	-14.07	10.5	3.5	16.292	2.989	-44.548	11	25	23.296	4.26	-5.194
9.5	8	7.378	0.14	-13.056	10.5	4	16.286	2.988	-38.857	11	30	23.016	4.408	-3.537